Electronic Supplementary Material (ESI) for CrystEngComm.
This journal is © The Royal Society of Chemistry 2020

Supplementary Information

Servann Hérou,[a] Maria Crespo [a]* and Magdalena Titirici [a]*

1. *Lignin characterisation*

1.1 2-Dimensional (^{13}C-^{1}H) Heteronuclear Single Quantum Coherence (HSQC)

The structural features of organosolv lignin were determined by HSQC-2D (^{13}C-^{1}H) NMR. This technique has recently shed light on lignin structures and has been used to analyse the interunit bonding units of various lignins extracted from biomass.[1,2,3,4,5] It also gives an indication on the amount of non-hydrolysed carbohydrates remaining linked on the lignin branches.

The organosolv lignin (OSL) shows interunits typically observed in hardwood lignins, as shown in Figure S1 and S2. Moreover, clear hydrocarbon peaks could not be observed even at lower contours levels assessing that the carbohydrate content of the organosolv product stays below detection level. The side-chain region of the 2D HSQC NMR spectra (left) (δC/δH 20-100/2.0-5.4) shows the high concentration of methoxyl groups (blue) observed at δC/δH 53.65-57.04/3.53-3.88.[1,5] The second most recognizable group (orange) (δC/δH 59.5-61.25/3.38-3.75) corresponds to the A_γ carbon atom (see Figure S1).[1,4] This shows the presence of numerous hydroxyl groups -OH in comparison to ketone -C=O groups. The green region (δC/δH 4.17-4.2 / 71.2-72.12) and yellow region (δC/δH 4.6-4.68/85.2-86.13) respectively correspond to the B_γ and B_α carbon in the B unit indicating the presence of β-β' linkages in the organosolv lignin. In native hardwood lignins, approx. 3% of linkages are β-β' linkages. A last region (δC/δH 4.55/80.65) corresponding to the A_β carbon is very weak and only appears at lower contours level especially on the ^{1}H spectrum (not shown on Figure S1). This low concentration of β-O-4 linkages in the organosolv lignin has also been shown by Zakzeski *et al*.[4] The DMSO peak (δC/δH 30-47/2.1-3.0) Is not shown on Figure S1 for more clarity.

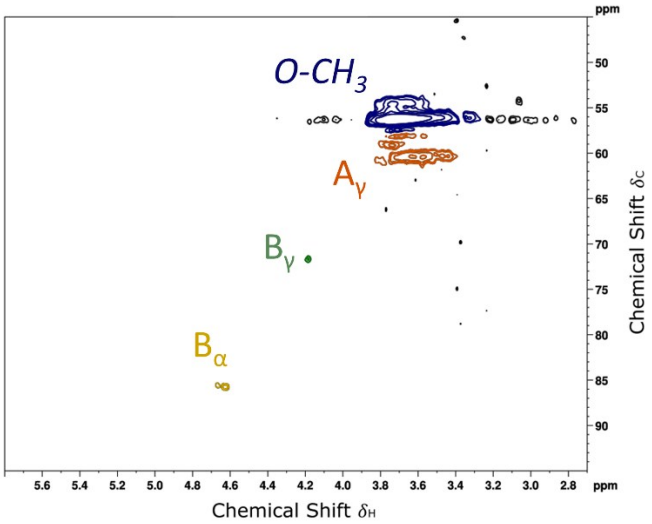

Figure S1: Aliphatic regions of the organosolv lignin, as detected by 2D HSQC NMR δC/δH 25-100/2.0-5.6

The aromatic region of the 2D HSQC NMR spectra (right) (δC/δH 70-150/5-9) shows a high concentration of syringyl units. The region (δC/δH 103.6-108.1/6.275-6.85) and 7 (δC/δH 107-107.5/7.23) corresponds respectively to the S_2 & S_6 carbon atoms as well as S'_2 & S'_6 carbon atoms.[1,6] At higher contours level we can observe the presence of guaicyl groups in much smaller concentration in region 8 (δC/δH 115-117/6.58-6.77), 9 (δC/δH 123.5/7.54-7.58), and 10 (δC/δH 110-113/7.16) respectively corresponding to the G_2 & G_6 carbon atoms, G'_6 and G'_2.

[a] *Chemical Engineering Department, Imperial College London, South Kensington, London SW7 2AZ*

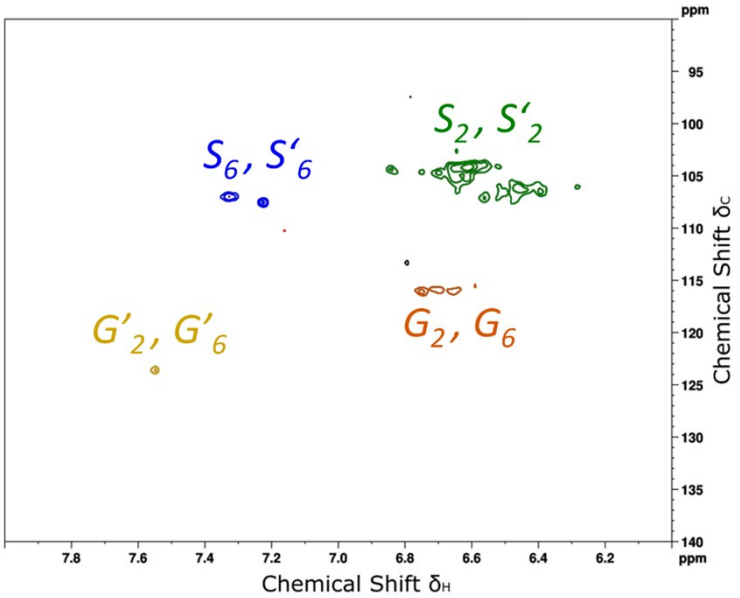

Figure S2: Aromatic regions of the organosolv lignin, as detected by 2D HSQC NMR (δC/δH 75-150/5.0-9.0)

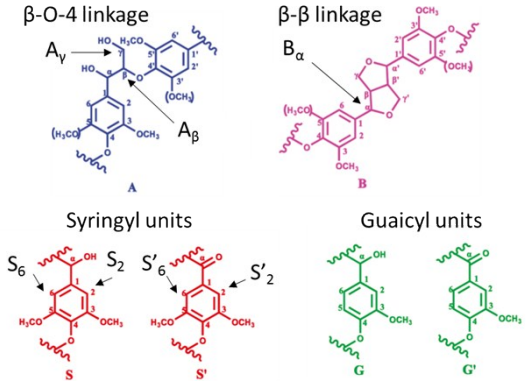

Figure S3: Annotations of the lignin structure present in the organosolv beech lignin. Reproduced from reference [1].

1.2 Hydroxyl-groups quantification via ^{31}P NMR

^{31}P-NMR was used to quantify the various hydroxyl groups contained in the organosolv lignin. The phosphitylation of hydroxyl groups by a phosphitylating agent, in the presence of an organic base, allows the phosphorous to react with all different hydroxyl groups present in the lignin.[7,8] The presence of a base such as pyridine, the conversion rate can reach close to 100% and this technique can be used with a phosphorous isotope to quantify the reacted oxygen sites (see Figure S4).

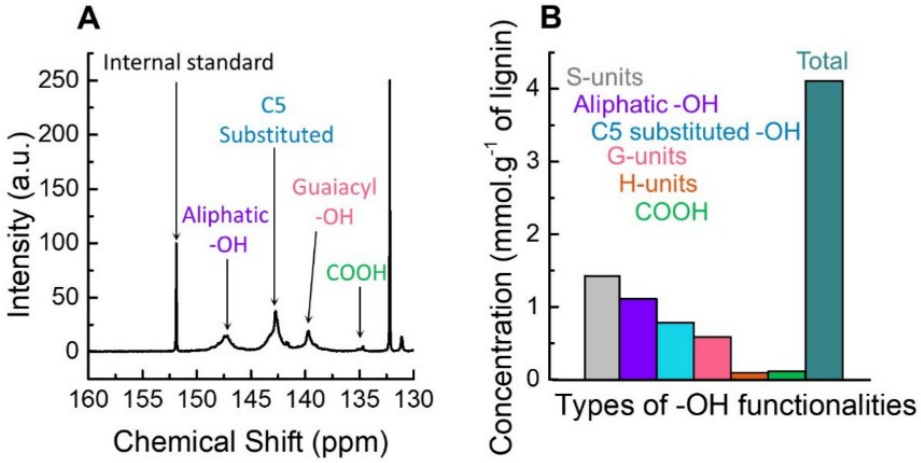

Figure S4: (a) ^{31}P-NMR spectrum and (b) Hydroxyl groups present in the organosolv lignin, as determined by ^{31}P-NMR

Figure S4a shows the ^{31}P-NMR spectrum of the OSL. The concentration of each oxygen group is calculated and shown on Figure S4b. As indicated by 2D-HSQC NMR, a higher quantity of syringyl -OH than guaicyl -OH groups (1.4 vs 0.6 mmol.g^{-1}) can be observed. This is one of the characteristics of hardwood lignins. The low carboxylic acid content (approximately 3% of the total oxygen concentration) indicates a low oxidation degree for this lignin, also predicted by the 2D-HSQC NMR. The ^{31}P-NMR spectrum also reveals the presence of C_5 substituted -OH which accounts for nearly 20% of the oxygen functional groups. This can be explained by the fact that C5 substituted -OH correspond to the bonds 5-5, *β*-5 and 4-O-5. In hardwood lignins, each of these linkages account for approximately 4.5%, 6% and 6.5% which makes a total of 17%. The very low concentration of H-units is also a main characteristic of dicotyledon hardwood plants, one of which is beech.

1.3 X-Ray Photo-electron spectroscopy (XPS)

The C1s spectra (Figure S5a) reveals the presence of sp^2 and sp^3 carbons corresponding respectively to the aromatic rings (284.4 eV) and the aliphatic chains (285.8 eV) of the organosolv lignin. At higher binding energies, the peaks can be attributed to the carbon-oxygen bonds and the functionalities found must match with the peaks fitting on the O1s spectrum (Figure S5b). The C-O peak at 286.85 eV, related to the C-OH peak at 532.3 eV on the O1s spectrum, it attributed to the phenolic -OH groups in S, G and H units, the aliphatic -OH on the A_α carbon. (see Figure S5.2) and the COOH groups. The O-C-O at 288.2 eV, related to the C-O-C on the O1s spectrum at 533.15 eV, is attributed to the numerous methoxyl groups present on the S and G-units of the lignin as well as the C5 substituted -OH groups. Finally, the C=O peak at 289.15 eV, related to the C=O peak at 531.5 eV and C-OH (in COOH) peak at 535.0 eV visible on the O1s spectrum, is attributed to the COOH groups. These results match with the ^{31}P-NMR which show that the aliphatic -OH, the phenolic compounds and the COOH functionalities account for 51% of the oxygen functionalities. The XPS reveals 52%. The methoxyl groups and the hydroxyl groups founds in the G-units where the carbon C5 is bonded in the 5-5, *β*-5 and 4-O-5 configurations (C5 substituted guaiacyl units), account for the rest 49%.

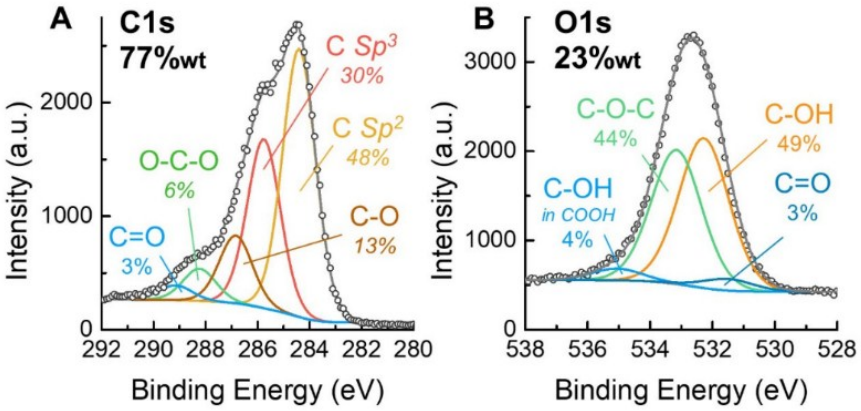

Figure S5: X-Ray Photo-electron spectroscopy (XPS) of the organosolv lignin. (a) C1s and (b) O1s spectra.

1.4 Gel Permeation Chromatography (GPC)

The molecular weight of the OSL was estimated by Gel Permeation Chromatography and calculated versus polystyrene (PS) as recommended by Lange, Tolbert et al.9,10 The OSL is highly dispersed with a molecular weight of Mw / Mn / PID of 4815 g.mol-1 / 3207 g.mol-1 / 1.5 versus polystyrene (see Figure S6). The polydispersity is quite low compared to the literature but the molecular weight is comparable.11,12

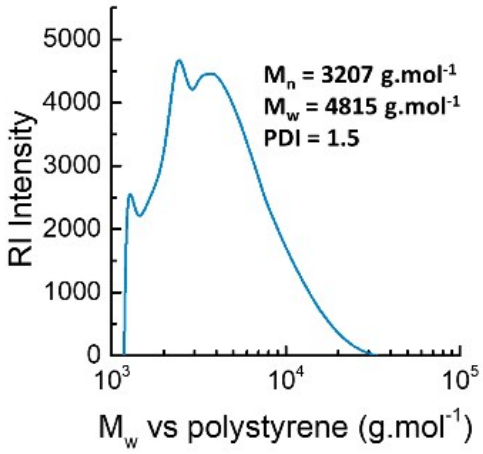

Figure S6: Gel Permeation Chromatography (GPC) molecular weight distribution versus polystyrene.

1.5 Thermal analysis

The thermogravimetric analysis (TGA) (Figure S7a) shows the decomposition curves under air and nitrogen atmosphere. Comparing the two curves provides information on oxidation behaviour of the sample. The shift of the weight loss at lower temperatures when the sample is tested under nitrogen atmosphere indicates a better thermal stability under air. This could be attributed to an oxidation of the lignin in air during the analysis despite the relatively high heating rate of 10°C.min^{-1}, which makes the lignin fragments less likely to gasify/degrade. Secondly, the degradation under air occurs within a relatively narrow temperature range (from approximately 370°C to 500°C), indicating the absence of volatiles which would gasify at lower temperatures than the lignin-char formed during pyrolysis.[13] Also the total weight loss at 500°C confirms the absence of inorganics (ashes) in this lignin, as expected from the organosolv extraction method. The third observation is related to the water content. Water tends to evaporate below 200°C in typical TGA experiments. The TGA curve shows a humidity below 5%, even though the OSL was stored under room temperature and not vacuum dried before the analysis. This result confirms that the oxygen contents reported in this chapter can be attributed to the lignin itself and not to adsorbed water. Finally, the thermal degradation of lignin in nitrogen atmosphere confirms the high carbon yield (33%wt at 1000°C) of this lignin compared to other cellulose of carbohydrates.[12] The glass transition temperature is usually characterised by a step in the heat flow observed on the DSC curve (Figure 7b). The T_g of the OSL could not be precisely determined due to the absence of clear step, even using a ramping rate of 20°C.min^{-1} (see Figure S7b). However, an estimation could be made by looking at the onset T_{on} and the end temperatures T_{end}. The T_g based on the endset is found around 100°C, which is in agreement with the glass transition temperatures reported in the literature.[14,15] Hardwood organosolv lignins exhibit generally lower T_gs than other types of lignin because of their low crosslinking degree. However, the absence of observable T_g at higher temperature could also be due to a potential in-situ oxidation of the lignin fragments as evidenced by TGA. Finally, the peak observed between 160°C and 200°C can be attributed to a melting of the lignin. At this temperature, no gasification is observed on the TGA curve and the brown powdered lignin becomes a viscous black fluid which solidifies as soon as the temperature drops below 150°C.

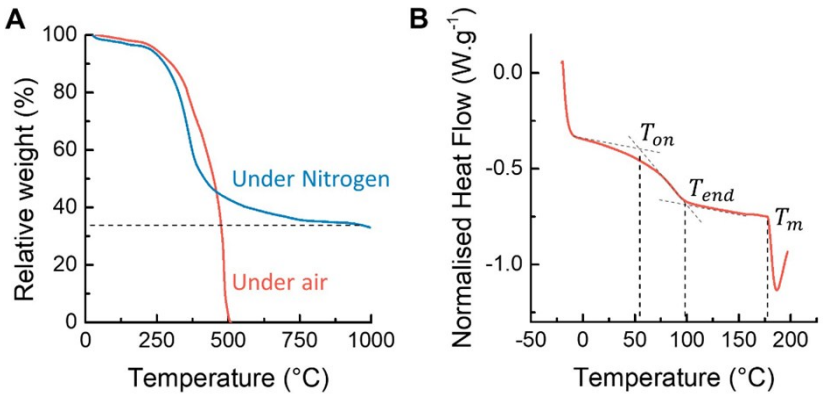

Figure S7: (a) Thermal gravimetric analysis of the organosolv lignin at 10 C.min^{-1} under air or nitrogen atmosphere. (b) Differential Scanning Calorimetry under air atmosphere at 20 C.min^{-1}

2. Results and Discussions

2.1 Morphology of the samples before pyrolysis

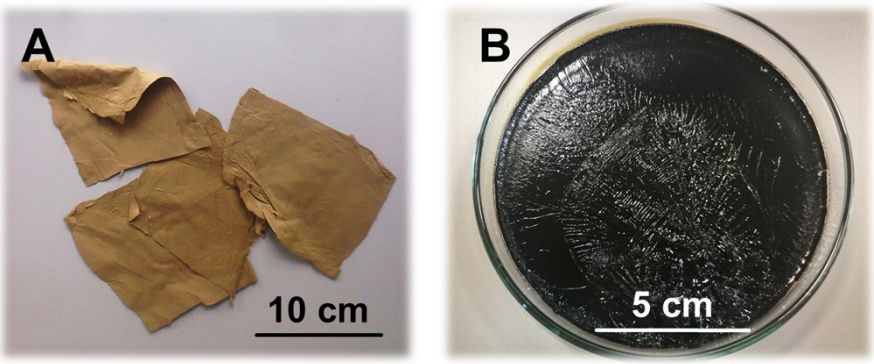

Figure S8: Pictures of the (a) Lignin-based nanofibre mat obtained after spinning and (b) dried cast film obtained after drying the spinning solution in a glass dish.

2.2 Morphology and characterisation of the carbon nanofibre after pyrolysis

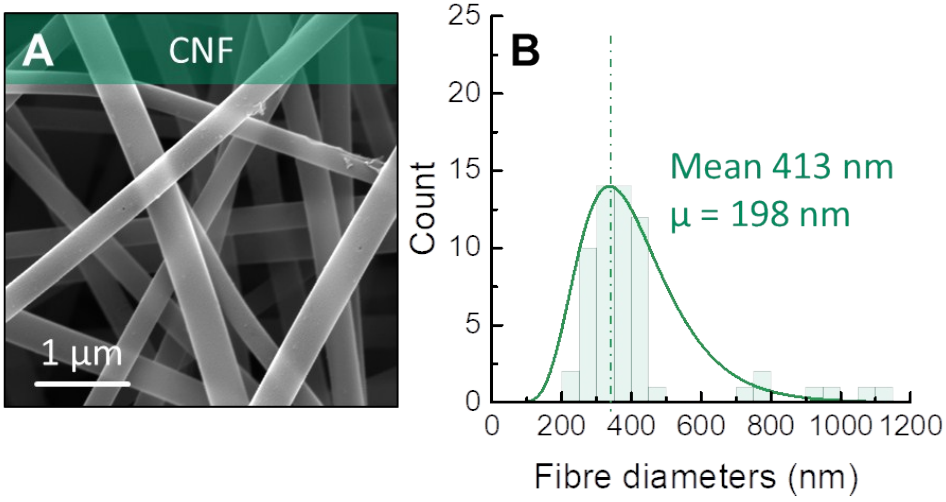

Figure S9: Scanning Electron Micrograph (SEM) of the carbon nanofibres obtained after pyrolysis and washing and (b) Diameter distribution obtained from the SEM image (60 counts) and fitted by a log normal distribution, showing an average of 413 nm and a standard deviation of 198 nm, due to the instabilities of the jet occurring during the spinning process.

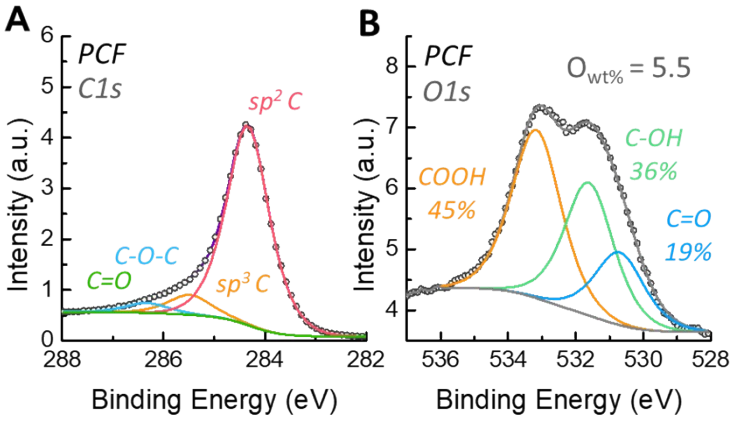

Figure S10: X-Ray Photoelectron Spectroscopy (XPS) of the lignin-based carbon nanofibres (PCF). (a) C1s spectrum and (b) O1s spectrum showing an oxygen percentage of 5.5wt%.

2.3 Sample yields

Table S1: Yield for the two different samples after carbonisation and washing

Sample	***Yield after carbonisation (wt%)***
CNF	*39 ± 2*
AC	*43 ± 2*

2.4 Electrochemical Characterisation

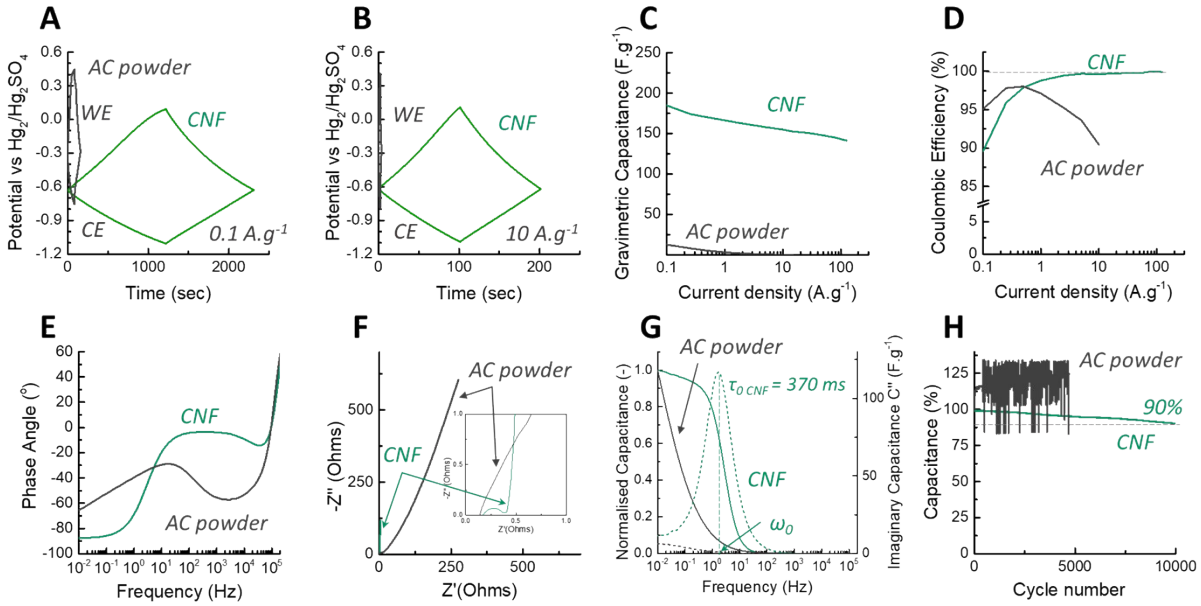

Figure S11: Galvanostatic Charge Discharge curves for both working and counter electrodes at (a) 0.1 A.g^{-1} and (b) 10 A.g^{-1}; (c) Capacitance retention showing 75% capacitance retention for PCF at 100 A.g^{-1}; (d) Coulombic efficiency calculated over the total cell charge and discharge; (e) Phase angle dependence on frequency as determined by Electrochemical Impedance spectroscopy (EIS); (f) Nyquist plot showing the real (Z') and imaginary (Z") components on the impedance (inset: Detailed Nyquist Plot at high frequency); (g) Normalised total and imaginary capacitance in function of the frequency, showing the characteristic relaxation time of each sample; (h) Cyclability at 10 A.g^{-1} showing noisy cyclability results for the cast AC powder because of its low capacitance value at 10 A.g^{-1} (see Fig S11c).

Additional References

1 T. Q. Yuan, S. N. Sun, F. Xu and R. C. Sun, *J. Agric. Food Chem.*, 2011, **59**, 10604–10614.

2 R. Samuel, Y. Pu, B. Raman and A. J. Ragauskas, *Appl. Biochem. Biotechnol.*, 2010, **162**, 62–74.

3 M. Sette, H. Lange and C. Crestini, *Comput. Struct. Biotechnol. J.*, 2013, **6**, e201303016.

4 J. Zakzeski, A. L. Jongerius, P. C. A. Bruijnincx and B. M. Weckhuysen, *ChemSusChem*, 2012, **5**, 1602–1609.

5 M. Hedenström, S. Wiklund-Lindström, T. Öman, F. Lu, L. Gerber, P. Schatz, B. Sundberg and J. Ralph, *Mol. Plant*, 2009, **2**, 933–942.

6 S. Yang, J.-L. Wen, T.-Q. Yuan and R.-C. Sun, *RSC Adv.*, 2014, **4**, 57996–58004.

7 A. Granata and D. S. Argyropoulos, *J. Agric. Food Chem.*, 1995, **43**, 1538–1544.

8 Y. Pu, S. Cao and A. J. Ragauskas, *Energy Environ. Sci.*, 2011, **4**, 3154–3166.

9 H. Lange, F. Rulli and C. Crestini, *ACS Sustain. Chem. Eng.*, 2016, **4**, 5167–5180.

10 J. R. Allison Tolbert, Hannah Akinosho, Ratayakorn Khunsupat, Amit K. Naskar, *Biofuels, Bioprod. Biorefining*, , DOI:10.1002/bbb.1500.

11 A. Abaecherli, M. Fasching, B. Hortling, J. Li, E. De Jong, U. M. R. Chimie, B. Agroparistech, S. Baumberger, A. Abaecherli, M. Fasching, G. Gellerstedt, R. Gosselink, B. Hortling, J. Li, B. Saake and E. De Jong, *Holzforschung*, 2007, **61**, 459–468.

12 C. G. Yoo, M. Li, X. Meng, Y. Pu and A. J. Ragauskas, *Green Chem.*, 2017, **19**, 2006–2016.

13 R. K. Sharma, J. B. Wooten, V. L. Baliga, X. Lin, W. G. Chan and M. R. Hajaligol, *Fuel*, 2004, **83**, 1469–1482.

14 Q. Sun, R. Khunsupat, K. Akato, J. Tao, N. Labbé, N. C. Gallego, J. J. Bozell, T. G. Rials, G. A. Tuskan, T. J. Tschaplinski, A. K. Naskar, Y. Pu and A. J. Ragauskas, *Green Chem.*, 2016, **18**, 5015–5024.

15 B. Hansen, P. Kusch, M. Schulze and B. Kamm, *J. Polym. Environ.*, 2016, **24**, 85–97.